NÖHÜ Müh. Bilim. Derg. / NOHU J. Eng. Sci., 2024; 13(4), 1452-1467

Niğde Ömer Halisdemir Üniversitesi Mühendislik Bilimleri Dergisi
Niğde Ömer Halisdemir University Journal of Engineering Sciences

Araştırma makalesi / Research article

www.dergipark.org.tr/tr/pub/ngumuh / www.dergipark.org.tr/en/pub/ngumuh

Inspection of the accuracy of fringe projection profilometry by using hybrid methods

Hibrit metotlar kullanarak ızgara projeksiyon profilemetrisinin doğruluğunun incelenmesi

Burak Özbay[1], **Zehra Saraç**[2,*]

[2,3] *Istanbul Medeniyet University, Electrical and Electronics Engineering Department, 34700, Istanbul, Türkiye*

Abstract

Fringe Projection Profilometry- FPP system is widely used for three-dimensional(3D) imaging. This system is promising. However, for the changing environmental conditions, the measurement object, system noise, and strong backlighting changing, it is difficult to obtain 3D image accurately by fringe analyzing methods such as Traditional Fourier Transform Method-TFFT in FPP System. Therefore, in this paper, the TFFT method is combined with various method and hybrid methods are formed. The aim is to investigate how these methods affect the accuracy of FPP system. To make this determination, from simulated fringe pattern, phase is calculated. Then the error values are obtained using these phase values. Consequently, it is seen from error results that TFFT with two Dimensional Empirical Mode Decomposition method-2D-EMD-FFT which gives the lowest error, is the most insensitive to the disruptive effects mentioned above. Moreover, it is the most stability and least affected by the geometric of the object under test.

Keywords: Fringe projection Profilometry, Hybrid methods, Fringe analysis, Accuracy

Öz

Izgara Projeksiyon Profilometri-FPP sistemi, üç boyutlu (3D) görüntüleme için yaygın olarak kullanılmaktadır. Bu sistem umut vericidir. Ancak değişen çevre koşulları, ölçüm nesnesi, sistem gürültüsü ve güçlü arka ışık değişimi nedeniyle FPP Sisteminde Geleneksel Fourier Dönüşüm Yöntemi-TFFT gibi saçak analiz yöntemleriyle doğru 3 boyutlu görüntü elde etmek zordur. Bu nedenle bu bildiride TFFT yöntemi çeşitli yöntemlerle birleştirilerek hibrit yöntemler oluşturulmuştur. Amaç bu yöntemlerin FPP sisteminin doğruluğunu nasıl etkilediğini araştırmaktır. Bu belirlemeyi yapmak için simüle edilmiş saçak deseninden faz hesaplanır. Daha sonra bu faz değerleri kullanılarak hata değerleri elde edilir. Sonuç olarak, hata sonuçlarından, en düşük hatayı veren İki Boyutlu Ampirik Mod Ayrıştırma yöntemi olan 2D-EMD-FFT'ye sahip TFFT'nin yukarıda bahsedilen bozucu etkilere en duyarsız olduğu görülmektedir. Üstelik test edilen nesnenin geometrisinden en az etkilenen ve en kararlı olanıdır.

Anahtar kelimeler: Izgara projeksiyon Profilometrisi, Hibrit yöntemler, Izgara analizi, Doğruluk

1 Introduction

FPP is a non-contact, non-destructive, reliable, and fast system. Moreover, it is a widely used application in industry as it allows for real-time measurement [1-6]. There are many factors to characterize the performance of FPP system, for example, speed, resolution, accuracy, reliability, cost, application scenario, etc. The most important among these factors is measurement accuracy of FPP system, which is not only determined by technical mechanisms, but is also affected by system components and setup, field of view, system calibration, geometric and surface properties of the measured objects, and ambient lighting [7-10]. The methods used in analyzing the fringe patterns obtained from such a system also influence the accuracy. They are greatly affected by noise, background, vibration, and so on.

Up to date, to reveal the factors mentioned above that affect the accuracy of a system, many studies of both experimental and simulation data have been performed. For example, Li et al. [7] analyzed how change the accuracy of FPP system by comparing several calibration methods.

Pérez et al. [11] obtained a 3D image of the surface of an oil painting with FPP system and attempted to determine the accuracy of the system experimentally. In this study it is used a four-step phase shift method and concluded that the accuracy of the system was one-tenth of a millimeter.

The higher order harmonics of the distorted fringe affect the accuracy of the FPP system as they cause errors in phase estimation. To solve this problem, Yin et al. [12] proposed a phase estimation method based on a neural network (PWPE-NN). They reported that the phase error caused by conventional methods in FPP systems that do not use a sinusoidal fringe pattern was eliminated by this method.

Lv et al. [13] have attempted a critical theoretical study to provide deep understanding and possible improvement of FPP system. Moreover, they investigated the theoretical effects on the accuracy of FPP, as well.

Nguyen et al. [8] aimed to investigate the accuracy of FPP and digital image correlation technique for 3D imaging.

---

* Sorumlu yazar / Corresponding author, e-posta / e-mail: zehra.sarac@medeniyet.edu.tr (Z. Saraç)

Geliş / Recieved: 25.03.2024 Kabul / Accepted: 19.09.2024 Yayımlanma / Published: 15.10.2024
doi: 10.28948/ngumuh.1458662

In their study, an experimental investigation into the accuracy comparison of two common 3D imaging systems has been presented: FPP and 3D digital image correlation (3D-DIC) technique. In their study, it was not revealed how the fringe analysis methods used in the system affect the accuracy of the system. By comparing the results of 3D imaging systems, the system that obtained the best image was determined experimentally.

López-Torres et al [9] proposed a method for identifying and removing shadows created by objects during 3D imaging of FPP and Wavelet Transform Profilometry (WTP). In the study, phase images, MSE (mean square error) and PSNR (peak signal-to-noise ratio) calculations, and execution times were presented. The results showed that the 3D imaging process was significantly improved with the removal of shadows.

In 2019, Xu et al. [10] presented a study for 3D imaging of translucent objects with FPP. Three major challenges, which are random errors, phase unwrapping failures, and geometric errors, form, when phase-shifting method for signal analyzing in FPP system is utilized to measure translucent objects. They presented a new method to overcome these challenges. The experimental results revealed that this method provides high accuracy.

In 1993, Perry et al. [1] showed that phase finding algorithms based on the phase shifting technique do not affect the accuracy of the FPP system even if edge effects, discontinuities, and noise are present.

Huang et al. [2] compared several fringe analysis methods used in FPP system in 2010. Although 2D-Windowed Fourier Transform (2D W-FFT) and 2D continuous wavelet transform (2D CWT) algorithms appear to be the most robust methods, they are time consuming and not suitable for real-time processing. All transformation methods performed poorly because of discontinuities in a phase map. In summary, it was concluded that the appropriate method should be selected according to the imaging requirements.

Kaya et al. [14] analyzed the interference fringes by the Hartley transform method (HTM) in the FPP system. It was concluded that although HTM had a short execution time, traditional Fourier Transform method (TFTM) provided a better 3D imaging.

In 2016, Li et al. [15] conducted a study on phase errors occurred when used shearlet transform (STM), EMD-TFFT (Emprical Mode Decomposition-TFFT), and wavelet transform (WTM) methods to calculate the phase in the FPP system.

Dursun et al. [16] investigated the performance of FPP system for 3D imaging by using some fringe analysis methods (the one-dimensional continuous wavelet transform (1D-CWT), 1D-CWT Gradient, TFFT). It was concluded that 1D-CWT has been better than TFFT and 1D-CWT gradient methods to find 3D profile in FPP system.

In 2010, Salvi et al. [17] presented a review study for showing the disadvantages and advantages of the fringe analysis methods, which are single phase shifting (SPS), multiple phase shifting (MPS), TFFT, and CWT.

As can be seen from the studies carried out so far, the accuracy of the FPP system is mostly affected by the signal analysis methods used in phase detection [18-28]. One of these methods is the TFFT method [1-2, 8, 19, 21, 29]. This method has some disadvantages such as edge and discontinuities effects, when used alone, as seen from the literature. In order to eliminate these disadvantages, in this study, hybrid methods, which are (1) TFFT with Savitzky–Golay (SG) Filter [30-32], (2) TFFT with Gaussian Window (W) [2, 33-34], (3) TFFT with 2D Empirical Mode Decomposition [35-38], and (4) TFFT with Modulation [39], were created. Here, a research study revealing how such hybrid methods affect the accuracy of the FPP system is presented for the first time. In addition, it is also revealed how the geometric shape of the object to be 3D imaged affects the phase found with these hybrid methods. Moreover, which method finds the 3D phase map more accurately is given by the error calculation. In this paper, accuracy of the FPP system is represented as phase error, which contains system, background, vibration noise etc.

As a result, it is seen that the TFFT method with 2D-EMD, which gives the lowest error for each object, is the most insensitive to noise. Moreover, it can be said that this hybrid method enables the imaging system to generate accurate results.

This work will be organized as follows. In the second part, the definitions of the hybrid fringe analysis methods used in the FPP system will be presented. In the third part, phases obtained from the fringe patterns (signal) taken from the FPP and phase errors will be shown. In the fourth part, the findings obtained in the results section will be compared and advantages and disadvantages of all hybrid methods will be given.

2 Principles of hybrid fringe analysis methods used in FPP systems

The Fringe Projection system (FPP) is illustrated in Figure 1 and the fringe pattern (signal) obtained from this system is given by Equation 1.

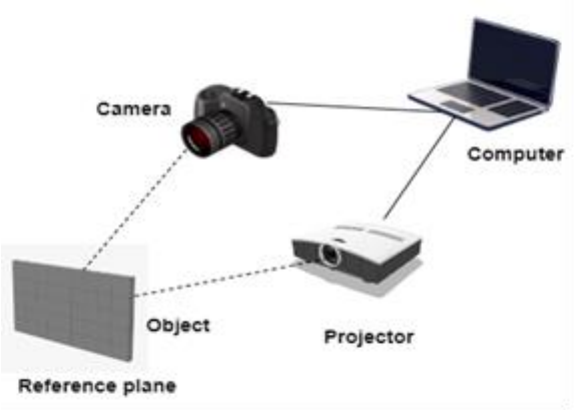

Figure 1. FPP System

2.1 Traditional fourier transform method-TFFT

Traditional Fourier Transform Method was used by Takeda in 1982 for signal (fringe) analysis [29] and a fringe pattern can be given by Equation 1.

$$i(x,y) = a(x,y) + b(x,y)\cos(2\pi f_o x + \phi(x,y)) \tag{1}$$

In the equation, a represents the background intensity distribution and b represents the fringe amplitude. ϕ is the phase that carries information about the measured profile. This pattern can also be written as in Equation 2.

$$\begin{aligned} i(x,y) \\ &= a(x,y) \\ &+ \frac{1}{2} b(x,y)\left\{\exp\left(i2\pi f_o x\right)\exp\left(i\phi(x,y)\right)\right. \\ &\left. + \exp\left(-i2\pi f_o x\right)\exp\left(-i\phi(x,y)\right)\right\} \end{aligned} \tag{2}$$

$$i(x,y) = a(x,y) + b(x,y)\cos(2\pi f_o x + \phi(x,y)) \tag{3}$$

$$c(x,y) = \frac{1}{2} b(x,y) exp(i\phi(x,y)) \tag{4}$$

Fast Fourier transform of Equation 3 with respect to x, is given in Equation 5.

$$I(\xi,y) = A(\xi,y) + C(\xi - \xi_o, y) + C^*(\xi + \xi_o, y) \tag{5}$$

f is the spatial frequency in the x direction. C^* is complex conjugate of the C.

The background $A(\xi,y)$ and the two frequency components at frequencies $\xi - \xi o$ and $\xi + \xi o$ of the signal are separated with the help of Fourier transform. With a band-pass filter (transfer function $H(\xi,y)$), only the $C(\xi - \xi_o, y)$ component is taken, as summarized in Equation 6.

$$C(\xi,y) = (\xi - \xi_o, y) = I(\xi,y)H(\xi,y) \tag{6}$$

Then *c*(*x*,*y*) is obtained by inverse Fourier transform.

$$c(x,y) = ifft\{I(\xi,y)H(\xi,y)\} \tag{7}$$

$$\phi(x,y) = arctan\frac{im\{c(x,y)\}}{re\{c(x,y)\}} \tag{8}$$

$im\{c(x,y)\}$; imaginary part of *c*(*x*,*y*) , $re\{c(x,y)\}$; is the real part. This discontinuous phase is between –π and +π. This phase is made continuous [*θ*(*x*,*y*)] using an appropriate unwrap algorithm. The phase is calculated for both the reference and the image captured with the object and the difference presented in Equation 9.

$$\Delta\theta = \theta_o - \theta_{ref} \tag{9}$$

Here θ_o, is the phase obtained from the unwrapped object image and θ_{ref} is the unwrap phase obtained from the reference image.

The flowchart used for the algorithm of this method is presented in Figure 2.

2.2 TFFT method with SG Filtering (SG–FFT)

A SG (Savitzky Golay) filter can be used to solve the problem of noise in the fringe pattern [30]. It is a simplified method for calculating the discrimination and smoothing of data with the least squares technique. The calculation speed of this method is better than the least squares technique. A major disadvantage of the method is that some of the initial and final data points cannot be corrected with the original SG method. However, Steinier et al. and Khan overcomes this problem [31].

The filter length or frame size N is odd, whereby it is assumed to be $N = 2M + 1$ ve $N \geq d + 1$, with $d =$ the degree of polynomial. x_n, if there is noisy sample, $n = 0, 1, \ldots, L - 1$ and if we convert them to smoothed outputs to y_n, $n = 0, 1, \ldots, L - 1$; then the data vector x, $n = L$ entry points and each side of x has N dimensions and M points; which replaces $x = [x_{-M}, \ldots\ldots, x_{-1}, x_0, x_1, \ldots\ldots x_M]^T$ with $x = [x_0, x_1, \ldots\ldots\ldots\ldots\ldots x_{L-1}]^T$. The output is described as follows. If we consider the state 1 output first; the first $M + 1$ output y_i is calculated.

$$y_i = b^{\,T}_{M-i}\, w(M), \qquad i = 0,1, \ldots M \tag{10}$$

The state vector is:

$$w(M) = \begin{bmatrix} x_{N-1} \\ . \\ \vdots \\ x_0 \end{bmatrix} \tag{11}$$

SG filtering is a popular method for smoothing data and calculating derivatives of noisy data based on local least squares fit of data with polynomials. SG filters are usually applied to equidistant data points, whereby each data point is based on fitting a polynomial of order n given the data in a (usually symmetric) k − m...k + m neighborhood of k (this range contains two m+1 data points). This filtering method was investigated in 1964 by Abraham Savitzky and Marcel J. E. Golay [30-32].

In this method, after SG Filtering, The TFFT is applied and the phase difference is obtained by Equation 9. The flow chart of SG-FFT hybrid method is presented in Figure 3.

2.3 TFFT with Gaussian Window (W-FFT)

In this section, an explanation will be given using the traditional Fourier transform method. The 1D Fourier transform can be described by the following equation

$$I(\xi) = \int_{-\infty}^{\infty} i(x)\, exp(-j\xi x)\, dx \tag{12}$$

$$i(x) = \frac{1}{2\pi}\int_{-\infty}^{\infty} I(\xi)\exp(j\xi x)\, d\xi \tag{13}$$

$I(\xi)$ is the Fourier transform of $i(x)$. The windowed Fourier transform of $i(x)$ and its inverse can be written as:

$$S(u,\xi)=\int_{-\infty}^{\infty} i(x)g(x-u)\,exp(-j\xi x)\,dx \tag{14}$$

$$i(x)=\frac{1}{2\pi}\int_{-\infty}^{\infty}\int_{-\infty}^{\infty} S(u,\xi)g(x-u)\,exp(j\xi x)\,d\xi\,du \tag{15}$$

$S(u,\xi)$ is known as the windowed Fourier spectrum; $g(x)$ is the window selected as the Gaussian function.

$$g(x)=exp(-\frac{x^2}{2\sigma^2}) \tag{16}$$

$g(x)$ is the parameter that controls the length of σ. With normal Fourier transform, $i(x)$is converted to $I(\xi)$, but there is only frequency information. Location information is almost never identifiable. The frequency information in the spectrum is obtained from $I(\xi)$, but it is not known where these frequencies are in relation to the signal. On the contrary, by using W-FFT it is possible to reach not only the frequency component, but also the positional information. This transformation technique offers two advantages:

1- Since W-FFT is performed over an area determined by the length of $g(x)$ (provided that their distance is greater than the effective radius of the Gaussian window), a signal at one location will not affect a signal at another location in spectral analysis

2- It is easier to study the spectrum of a signal in a local field than to study the entire field spectrum, therefore, the W-FFT spectrum is easier to interpret

The spectrum of W-FFT can be studied in two ways:

1- By performing thresholding, low amplitude spectral components are reset, thus, the noise spreads over the entire spectrum. As noise disappears, a high quality signal can be reconstructed.

2- The frequency corresponding to the peak of the spectrum is considered the local frequency or instantaneous frequency. This approximation shows that the spectrum of the signal in a local area is simple and consists of only one frequency.

Based on W-FFT, two different approaches are possible for fringe demodulation called the windowed Fourier filtering (W-FFT) method and the windowed Fourier ridges (W-FFR) method. W-FFT filters the fringe pattern in the windowed Fourier space and W-FFR provides the best match between the fringe pattern and computer-generated windowed exponentials. In this study The W-FFT method is used [33-34].

As seen in Equation 2, the fringe pattern consists of two exponential functions and background density. When we consider the carrier frequency, there are three spectrum components in the frequency domain. The W-FFT of Equation 2 can be written as follows:

$$i(x)=\frac{1}{2\pi}\int_{-\infty}^{\infty}\{[i(x)\otimes h(x,\xi)]\otimes h(x,\xi)\}d\xi \tag{17}$$

$h(x,\xi)=g(x)\exp(j\xi x)$ taken as and $\otimes$ shows the convolution. If W-FFT is written in a specific region, it can be expressed by the equation given below:

$$\overline{\imath(x)}=\frac{1}{2\pi}\int_{a}^{b}[i(x)\otimes h(x,\xi)]\otimes h(x,\xi)d\xi \tag{18}$$

If $|i(x)\otimes h(x,\xi)|$ is less than a certain threshold value, it behaves as noise and is removed at reset. Threshold selection is important. The integral boundaries are between *a* and *b*. Thus, in the 2D spectrum, only the spectrum of the positive frequency portion is obtained from the three frequency components. In this case, 2D phase can also be written as follows:

$$\phi(x,y)=arctan\frac{im\{\overline{\imath(x,y)}\}}{re\{\overline{\imath(x,y)}\}} \tag{19}$$

The phase difference is obtained by substituting this phase in Equation 9. The flow diagram of the W-FFT method is presented in Figure 4:

2.4 TFFT method with 2D-Empirical Mode Decomposition (2D-EMD-FFT)

For the EMD method developed by Huang et al., the non-stationary signal is made stationary using the signal Hilbert-Huang transform [35]. Here it is considered that the signal can have more than one different simultaneous mode of modals (intrinsic mode functions [IMFs]). Based on this idea, a complex signal can be decomposed into the sum of several IMFs and one residue, which can be easily modelled. Here, IMFs are extracted based on the local characteristic scale of the complex signal. In EMD, the IMF and the residuals are used to obtain the original signal without loss of information and error. When creating IMFs, they must meet certain conditions. For example, the number of zero crossings must be equal to the number of endpoints or the difference between them must be one. The other condition is that the mean value of the upper envelope and lower envelope must be zero for each instance of the sign. Interpolation of upper envelope maximum points are found by interpolation of the minimum points in the lower envelope. The resulting IMFs are nearly orthogonal to each other [36]. They describe 1D- EMD and [37-38].2D-EMD and here, 2D- IMF is used. First, the IMFs of the *i*(*x*,y) sign are found, then the numbered IMFs are taken, they are added together, and the filtered signal becomes as in Equation 3. This signal is in the order of the traditional Fourier transform and the phase difference is obtained by applying the operations in Equations 5 and 9.

The flow diagram of the 2D-EMD-FFT method is presented in Figure 5.

2.5 TFFT method with modulation (GPM-FFT)

In this method, *i*(*x*) and *g*(x) Gaussian windows are multiplied. Then, the spatial frequency plane is passed with Fourier transform. Afterwards, the steps in the traditional Fourier transform method are applied and the phase is obtained. The equations of the method are presented below. The multiplication of the interference pattern and the Gaussian window obtained is as follows:

$$f(x) = i(x)\, g(x) \tag{20}$$

The multiplication represents the modulation in the spatial plane. By taking the Fourier transform, Equation 21, the modulation process is obtained in the frequency plane.

$$F(\xi) = \int_{-\infty}^{\infty} f(x)\, exp(-j\xi x)\, dx \tag{21}$$

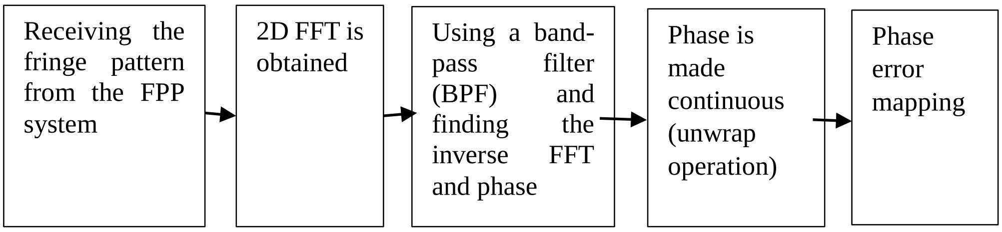

Figure 2. Flowchart of TFFT Method

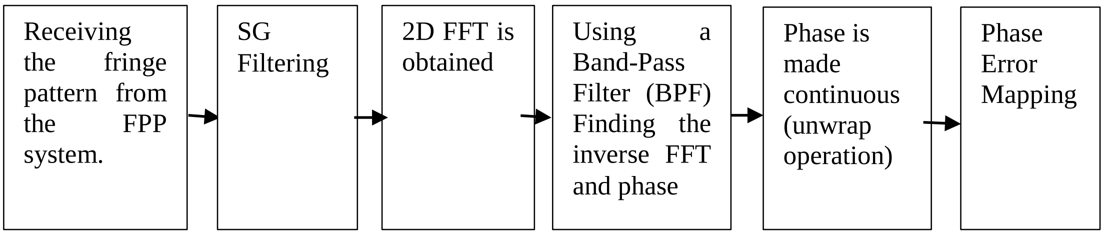

Figure 3. Flowchart of the SG-FFT Method

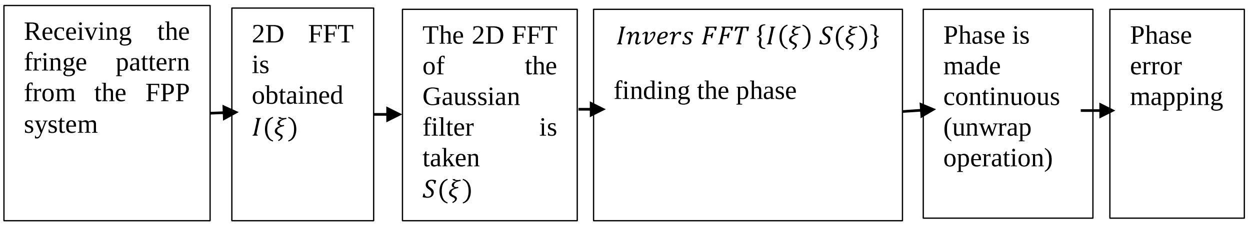

Figure 4. Flowchart of the W-FFT method.

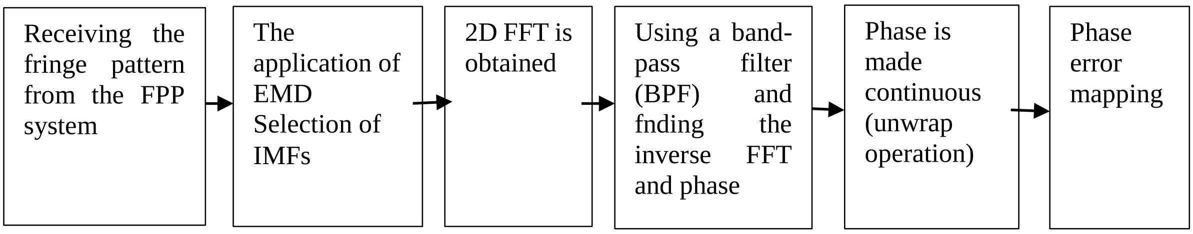

Figure 5. Flowchart of the 2D-EMD-FFT method.

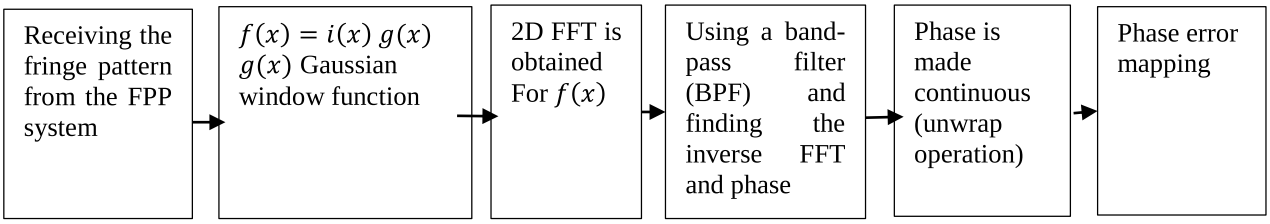

Figure 6. Flowchart of GPM-FFT Method

Then the signal with edge effects is removed and high frequency noise components eliminated. The signal is processed with the conventional Fourier transform (as in Equation 6) and the phase difference is obtained with Equation 9.

The flow chart of the method is illustrated in Figure 6.

3 Simulations and presentation of results

In this section, simulation studies and their results will be presented. Three objects were selected to simulate the signal received from the 3D imaging system (FPP). It is assumed that a 3D image of the hemisphere, cone, and complex crested objects shown in Figure 7 are obtained from this system. The 2D fringe pattern captured by the camera in such a system (commonly a charge coupled device [CCD] is used) can be mathematically given by the Equation 22:

$$i(x,y) = a(x,y) + b(x,y)\,cos\big(2\pi f_o x + \phi(x,y)\big) + noise \qquad (22)$$

The $\phi(x,y)$ phase in this equation is the phase information derived from the mathematical expressions of the selected objects.

$i(x,y)$; is produced as an image with 512x512 pixels. This means camera resolution is accepted 512x512 pixels.

In $i(x,y)$, $\phi(x,y)$ is produced as a 512x512 pixel image and is represented by Equation 23 for the hemisphere:

$$\phi(x,y) = Re\left\{10\sqrt{\left(1-\frac{(x-256)^2+(y-256)^2}{240^2}\right)}\right\} \qquad (23)$$

Here, $Re\{\ \}$ represents the real part of the complex expression. Spatial frequency of the fringe pattern is set to $f_0 = 1/16$. $a(x,y)$ background intensity, it is defined as 1. $b(x,y)$ modulation intensity is 1. White Gaussian noise (WGN) was selected as the noise and the power of the noise samples is specified as scalar and is taken as 8 dBW.

The original phase $\phi(x,y)$ for the actual hemisphere obtained by using equation 23 is given in Figure 7(a).

For cone shapes, the phase expression in Equation 22 is taken as in Equation 24. However, phases less than 200 are taken as zero and replaced in phase (Equation 24):

$$\phi(x,y) = 50\left(1-\frac{\sqrt{(x-256)^2+(y-256)^2}}{200}\right) \qquad (24)$$

The original phase $\phi(x,y)$ for the actual cone obtained by using equation 24 is given in Figure 7(b).

The phase expression in Equation 22 is taken as in Equation 25 for a complex crested shape:

$$\phi(x,y) = 3\,(1-x)^2\, e^{(-x^2-(y+1)^2)} - 10\left(\frac{x}{5} - x^3 - y^5\right) e^{(-x^2-y^2)} - \frac{1}{3} e^{(-(x+1)^2-y^2)} \qquad (25)$$

The original phase $\phi(x,y)$ for the actual complex crested shape obtained by using equation 25 is given in Figure 7(c).

Fringe patterns of objects obtained from the 3D FPP using these objects and the simulation results are presented in Figure 8.

In addition, the simulated reference image (using Equation 26) obtained from the FPP without placing the object is presented in Figure 9.

$$i_{ref}(x,y) = a(x,y) + b(x,y)\,cos(2\pi f_o x) + noise \qquad (26)$$

The unwrap phases (ϕ_0, ϕ_{ref}) are calculated by using the simulated pattern $i(x,y)$ and $i_{ref}(x,y)$ obtained from the FPP for a hemispherical object. The noisy phase map ($\phi_{son}(x,y)$) is obtained by Equation 27.

$$\phi_{son}(x,y) = \phi_0(x,y) - \phi_{ref}(x,y) \qquad (27)$$

Firstly, $\phi_{son}(x,y)$ is found for hemispherical object by TFFT in Figure 10(a). The result obtained by SG-FFT is given in Figure 10(b). The results calculated by using W-FFT, 2D-EMD-FFT, and GPM-FFT hybrid methods are illustrated in (c), (d), and (e), respectively.

To compare which of these methods has the least noise, the error (error=e) values are calculated by Equation 28. In here, $\phi(x,y)$ is calculated by Equation.23 for hemispherical object. The error values are presented in Figure 11 for (a) TFFT, (b) SG-FFT, (c) W-FFT, (d) 2D-EMD-FFT, and (e) GPM-FFT hybrid methods, respectively.

$$e = \phi_{son}(x,y) - \phi(x,y) \qquad (28)$$

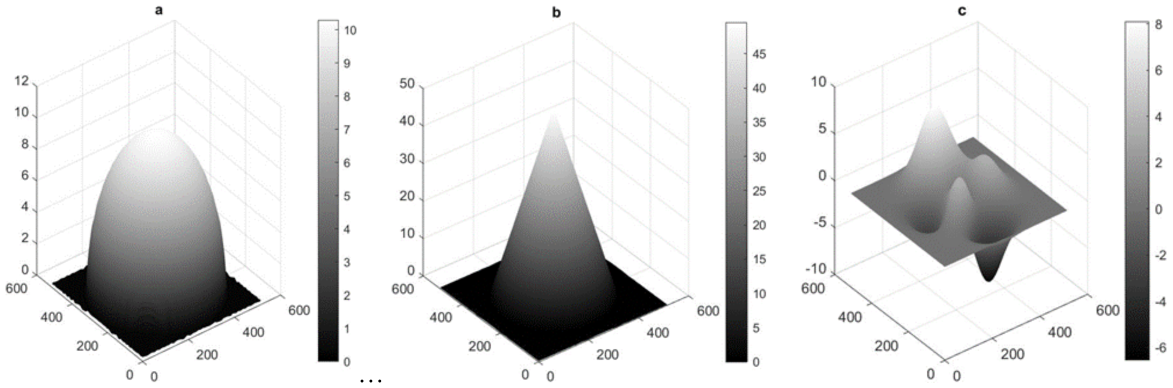

Figure 7. The original phases for (a) hemisphere, (b) cone, and (c) complex crested objects.

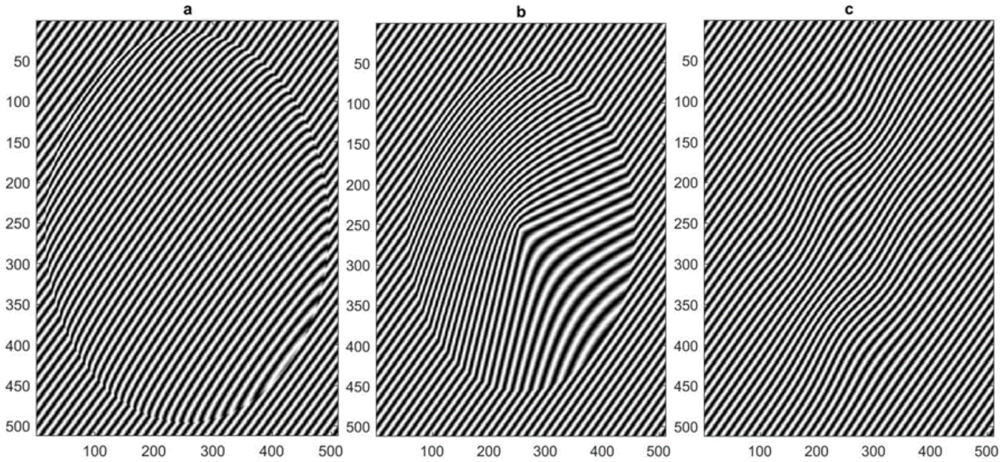

Figure 8. 2D images of simulated fringe patterns using relevant phases (bodies) for (a) hemisphere, (b) cone, and (c) complex crested shape.

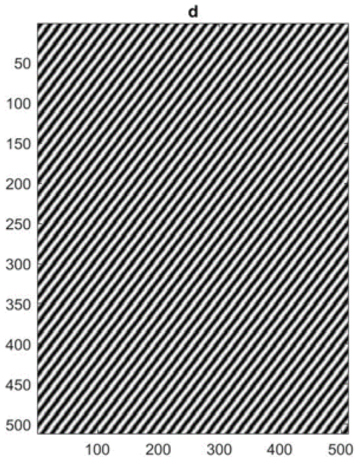

Figure 9. The image of fringe pattern simulated using reference $i_{ref}(x, y)$.

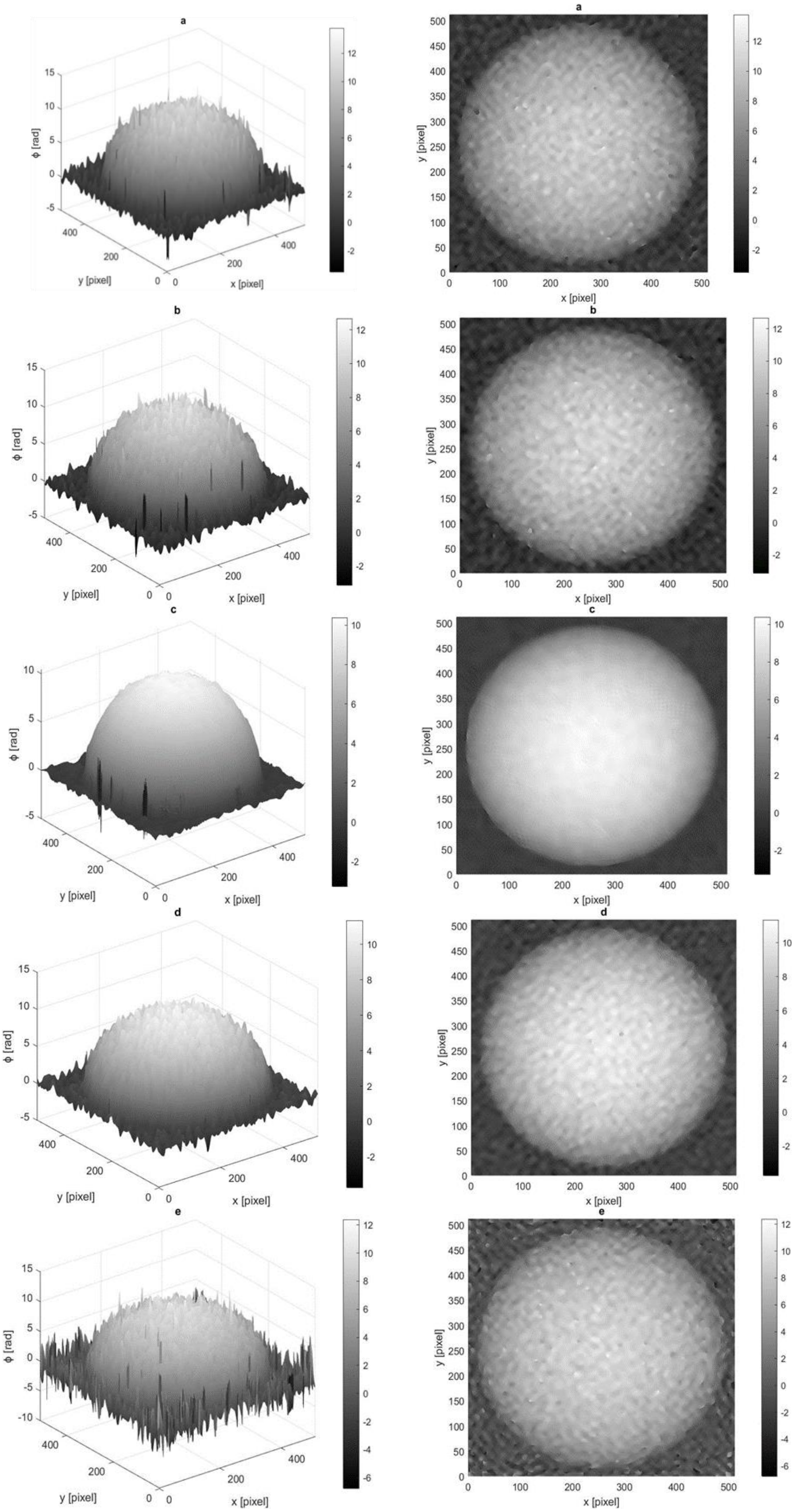

Figure 10. Phase maps, $\phi_{son}(x, y)$(noisy phase), obtained using (a) TFFT, (b) SG-FFT, (c) W-FFT, (d) 2D-EMD-FFT, and (e) GPM-FFT hybrid methods from simulated fringe patterns for the hemispherical object.

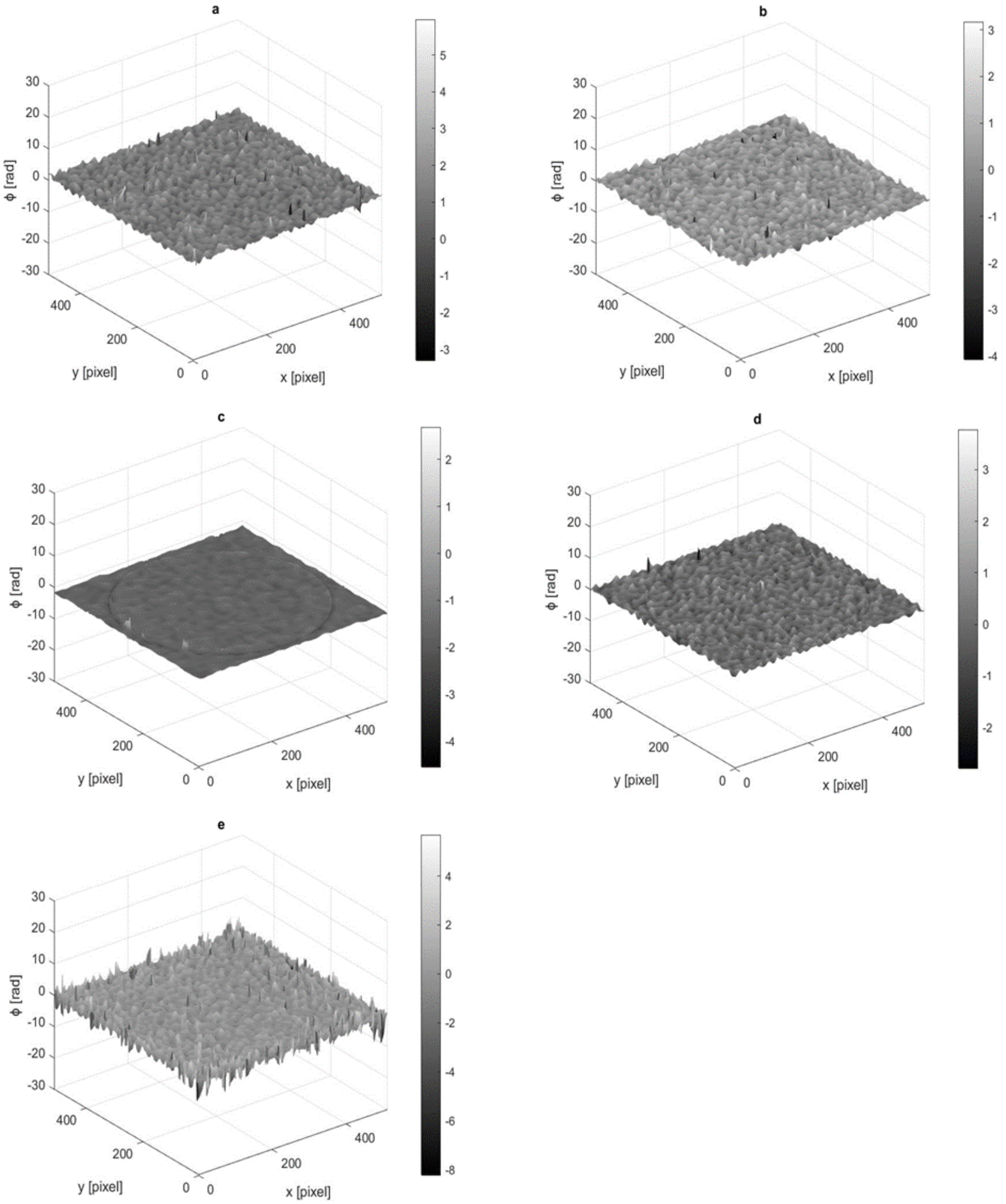

Figure 11. Error maps obtained by Equation 28 between actual phase and noisy phase. $\phi_{\text{son}}(x, y)$ was obtained with (a) TFFT, (b) SG-FFT, (c) W-FFT, (d) 2D-EMD-FFT, and (e) GPM-FFT hybrid methods from the simulated fringe pattern images for the hemispherical object.

The unwrap phase, $\phi_{son}(x, y)$, is found for cone object by TFFT in Figure 12(a) by using Equation 27. The result obtained by SG-FFT is given in Figure 12(b). The results calculated by using W-FFT, 2D-EMD-FFT, and GPM-FFT hybrid methods are illustrated in (c), (d), and (e), respectively.

To compare which of these methods has the least noise, the error (error=e) values are calculated by Equation 28. In here, $\phi(x, y)$ is calculated by Equation.24 for cone object. The error values are presented in Figure 13 for (a) TFFT, (b) SG-FFT, (c) W-FFT, (d) 2D-EMD-FFT, and (e) GPM-FFT hybrid methods, respectively.

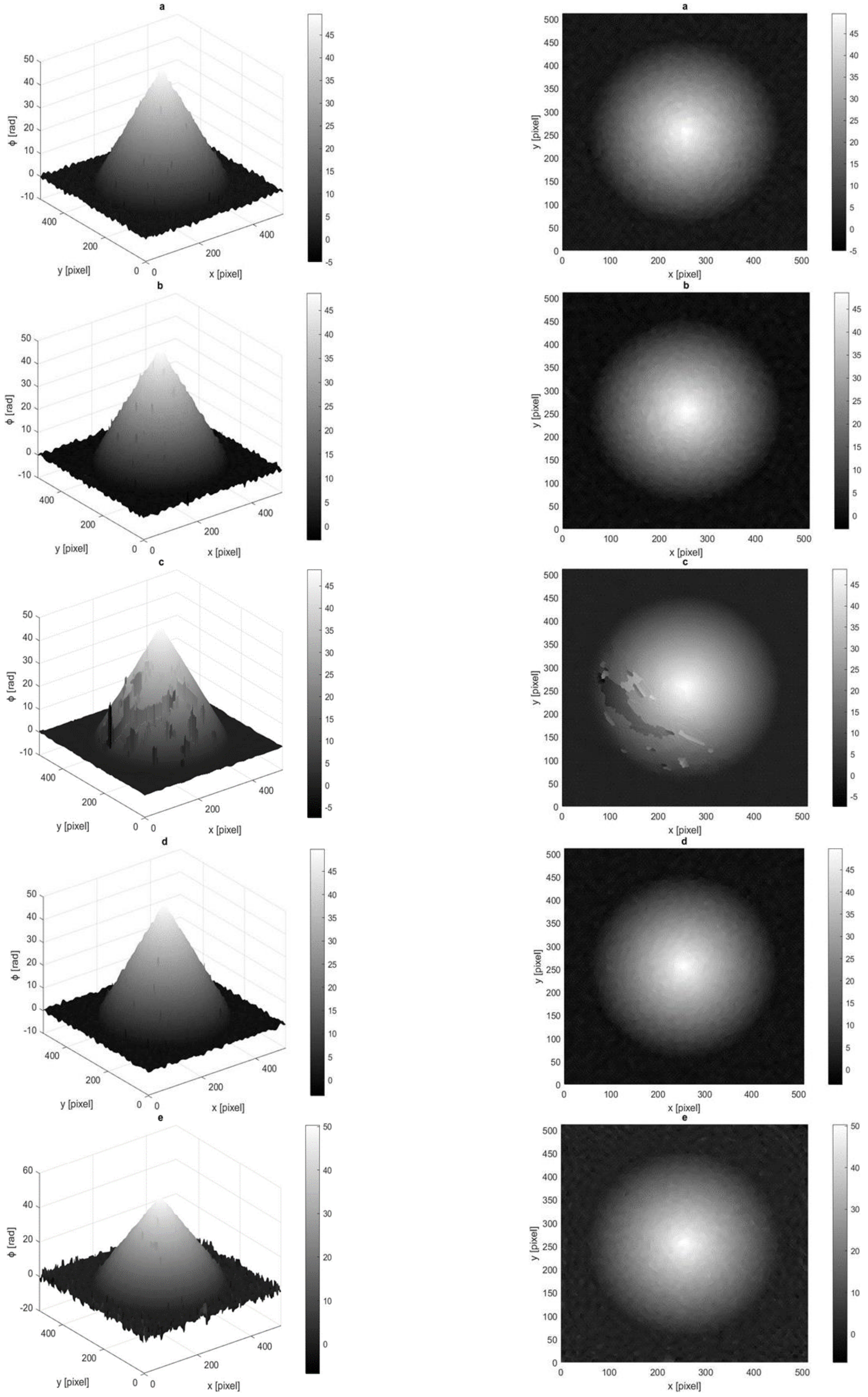

Figure 12. Phase maps, $\phi_{son}(x, y)$(noisy phase), obtained using (a) TFFT, (b) SG-FFT, (c) W-FFT, (d) 2D-EMD-FFT, and (e) GPM-FFT hybrid methods from the simulated fringe pattern images for the cone object.

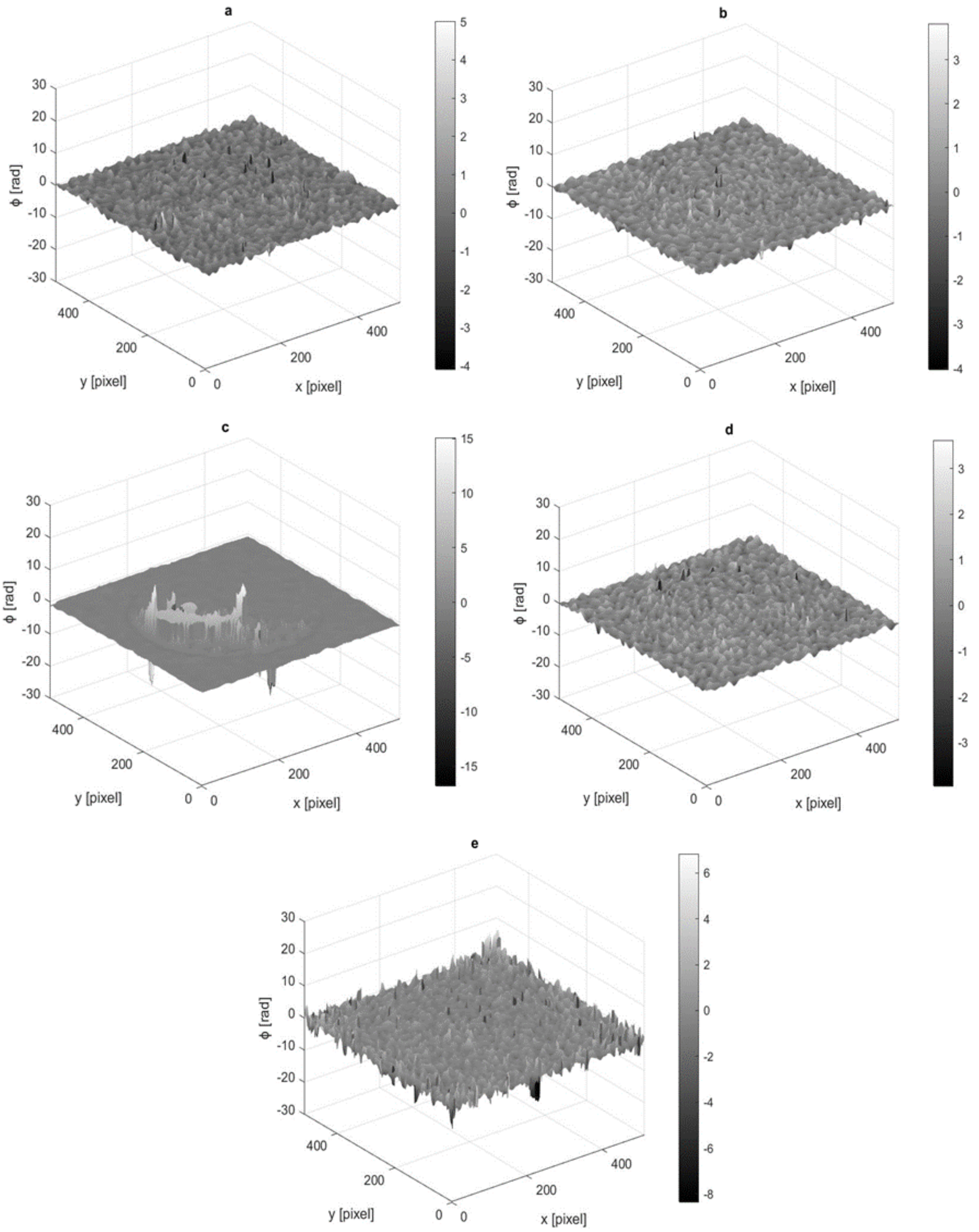

Figure 13. Error maps obtained by Equation 28 between actual phase and noisy phase, $\phi_{son}(x,y)$ obtained using (a) TFFT, (b) SG-FFT, (c) W-FFT, (d) 2D-EMD-FFT, and (e) GPM-FFT hybrid methods from the simulated fringe pattern images for the cone object.

The unwrap phase $\phi_{son}(x,y)$ is found for complex crested object by TFFT in Figure 14(a). The result obtained by SG-FFT is given in Figure 14(b). The results obtained by using W-FFT, 2D-EMD-FFT, and GPM-FFT methods are illustrated in (c), (d), and (e), respectively.

To compare which of these methods has the least noise, the error (error=e) values are calculated by Equation 28. In here, $\phi(x,y)$ is calculated by Eq.25 for complex crested object. The error values were presented in Figure 15 for (a)TFFT, (b) SG-FFT, (c) W-FFT, (d) 2D-EMD-FFT, and (e)GPM-FFT hybrid methods, respectively.

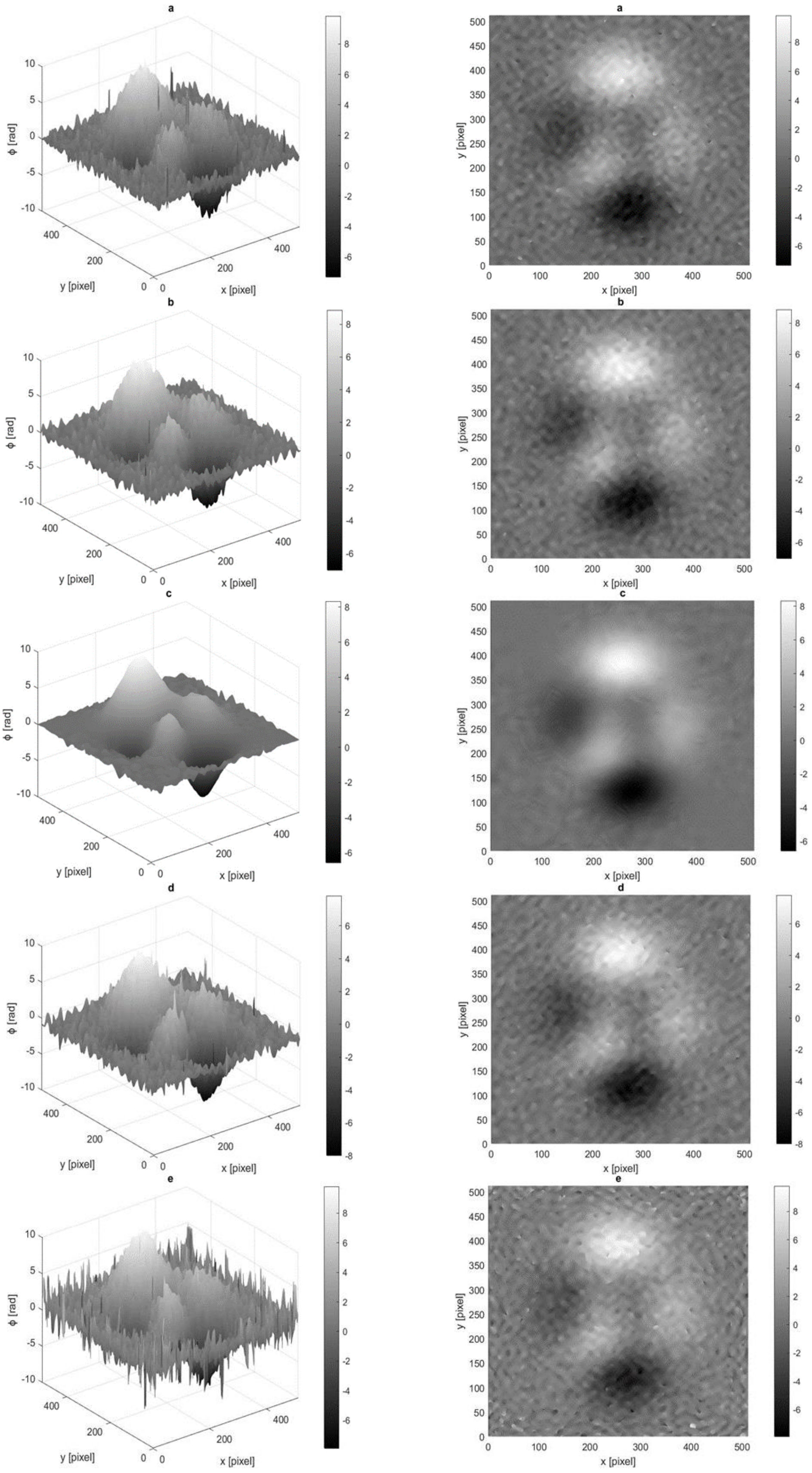

Figure 14. Phase maps, $\phi_{son}(x, y)$(noisy phase), obtained using (a) TFFT, (b) SG-FFT, (c) W-FFT, (d) 2D-EMD-FFT, and (e) GPM-FFT hybrid methods, from the simulated fringe pattern images for the complex crested object.

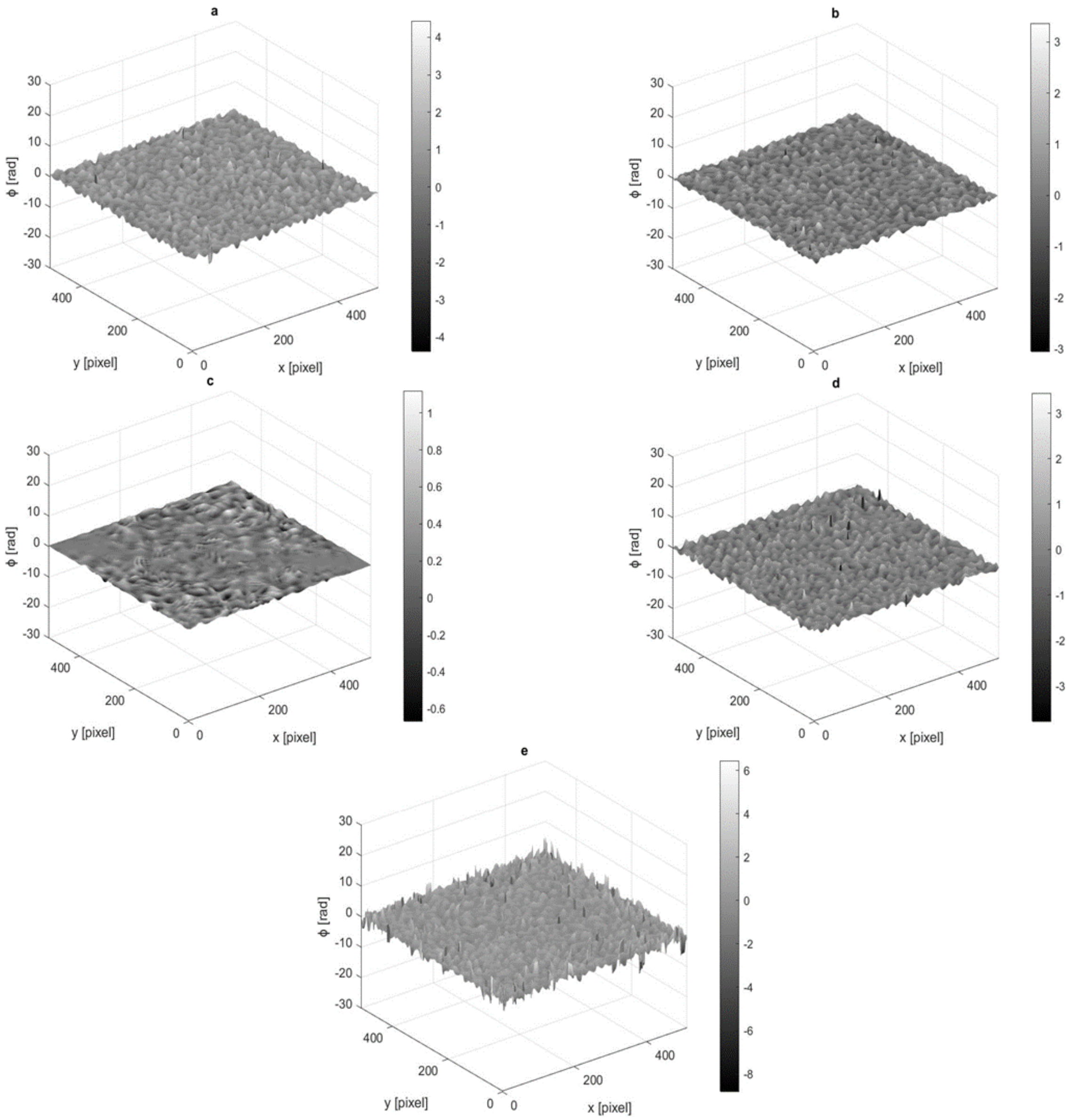

Figure 15. Error maps calculated by Equation 28 between actual phase and noisy phase, $\phi_{son}(x, y)$ obtained using (a) TFFT, (b) SG-FFT, (c) W-FFT, (d) 2D-EMD-FFT, and (e) GPM-FFT hybrid methods from the simulated fringe pattern images for the complex crested object.

4 Conclusions and discussion

In this paper, accuracy parameter, which show the performance of FPP system, is inspected and represented as phase error, which contains system, background, vibration noise etc. In addition, it is mostly affected by the fringe analysis methods used in phase detection. One of these methods, which has some disadvantages such as edge and discontinuities effects, is TFFT. In this paper, because of this, the TFFT is combined with some method and hybrid methods which are called as SG-FFT, W-FFT, 2D-EMD-FFT, and GPM-FFT are formed. Here, the purpose is to show how such hybrid methods affect the accuracy of the system for the first time. In addition, it reveals how the geometric shape of measured object affects the phase obtained by these hybrid methods. In same time, which method gives the 3D phase map more accurately is presented by the error calculation. It was concluded from phase and its error values obtained for three objects (hemispherical, cone, complex crested objects) as follows:

1- The phase and error values obtained for hemispherical object are presented in Figure 10 and 11, respectively. As can be seen from Figures, the most accurate phase result for such an object is obtained by the 2D-EMD-FFT method (see Figure 10(d), 11(d)). If the methods are ranked from most to least accurate, they would be as follows: W-FFT (see Figure 10(c) ,11(c)), SG-FFT (see Figure 10(b), 11(b)), TFFT (see Figure 10(a), 11(a)) and lastly GPM-FFT (see Figure 10(e), 11(e)). As already established, the phase information obtained from the FPP system with the specified methods is greatly affected by system noise, background, vibration etc. Here, it can be said that 2D-EMD-FFT results (see Figure 10(d) and 11(d)) are better because this method eliminates especially the background noise.

The best phase and error results for hemispherical object are obtained by 2D-EMD-FFT hybrid method.

2- The results obtained for the cone object are given in Figure 12 and 13, respectively. As with the hemispherical object, 2D-EMD-FFT is the method that gives the most accurate results (see Figure 12(d), 13(d)) and presents the least error. The second most accurate method is SG-FFT (look at Figure 12(b), 13(b)) followed by TFFT (Figure 12(a),13(a)), GPM-FFT (Figure 12(e), 13(e)), and W-FFT (see Figure 12(c) and 13(c)). As expected, the 2D-EMD-FFT method gives the best results.

The best phase and error results for cone are obtained by 2D-EMD-FFT hybrid method again.

3- Considering the 2D and 3D phase (see Figure 14) and the error values (see Figure 15) calculated using the fringe patterns obtained from FPP system for complex crested shape, W-FFT gives the best results (see Figure 14(c), 15(c)). The smallest error is observed with this method (see Figure 15(c)). W-FFT is followed by 2D-EMD-FFT (look at Figure 14(d), 15(d)) and SG-FFT (see Figure 14(b) and 15(b)) in terms of effectiveness. TFFT (look at Figure 14(a), 15(a)) is better in every way than GPM-FFT (see Figure 14(e), 15(e)).

Although the best phase and error results for complex crested shape are obtained by W-FFT hybrid Method, 2D-EMD-FFT follows it with very small difference. This means that 2D-EMD-FFT is very stability. In every situation it gives more accurate result.

As a result, it is seen that the effectiveness of hybrid methods depends on the surface properties, material and geometric shape of the measured object.

First result is that the 2D-EMD-FFT method presents the least error in all conditions and is least affected from the changing environmental conditions, the geometry and surface structure of measured object.

Second result is that SG-FFT hybrid method follows 2D-EMD-FFT, but sometimes may reduce the accuracy of the system directly. Because SG Filter makes the smoothing process, which affects the properties of the surface of tested object.

Third result is that GPM-FFT hybrid method gives the greatest error unconditionally and reduces the accuracy of the FPP system. It is concluded that GPM-FFT is not suitable for fringe analysis.

The last result is that W-FFT is not a method that increases the accuracy of the system as much as suggested in the literature [2]. and it does not show stability. In addition, it can reduce very much the accuracy of the system depending on the geometric shape of the object being measured.

Conflicts of Interest

No conflict of interest was declared by the authors.

Similarity Rate (iThenticate): 16%

References

[1] K. E. Perry, J. McKelvie, A comparison of phase-shifting and Fourier methods in the analysis of discontinuous fringe patterns. Optics and Lasers in Engineering, 19, 269–284, 1993. https://doi.org/10.1016/0143-8166(93)90068-V.

[2] L. Huang, Q. Kemao, B. Pan, and A. K. Asundi, Comparison of Fourier transform, windowed Fourier transform, and wavelet transform methods for phase extraction from a single fringe pattern in fringe projection profilometry. Optics and Lasers in Engineering, 48, 141-148, 2010. https://doi.org/10.1016/j.optlaseng.2009.04.003.

[3] P. S. Huang, C. Zhang, and F. P. Chiang, High-speed 3D shape measurement based on digital fringe projection. Optical Engineering, 42, 163-169, 2003. https://doi.org/10.1117/1.1525272.

[4] Z. H. Zhang, Review of single-shot 3D shape measurement by phase calculation-based fringe projection techniques, Optics and Lasers in Engineering, 50 106–1097, 2012. https://doi.org/10.1016/j.optlaseng.2012.01.007

[5] P. Zhou, J. Zhu, X. Su, Z. You, H. Jing, C. Xiao, and M. Zhong, Experimental study of temporal-spatial binary pattern projection for 3D shape acquisition. Applied Optics, 56, 2995–3003, 2017. https://doi.org/10.1364/AO.56.002995.

[6] A. Martínez, J.A. Rayas, R.R. Cordero, D. Balieiro, and F. Labbe, Leaf cuticle topography retrieved by using fringe projection. Optics and Lasers in Engineering, 50, 231-235, 2012. https://doi.org/10.1016/j.optlaseng.2011.08.011.

[7] X. Li, Z. Zhang, and C. Yang, Reconstruction method for fringe projection profilometry based on light beams. Applied Optics, 55(34), 9895-9906, 2016. https://doi.org/10.1364/AO.55.009895.

[8] H. Nguyen, J. Liang, Y. Wang, and A. Wang, Accuracy assessment of fringe projection profilometry and digital image correlation techniques for three-dimensional shape measurements. Journal of Physics: Photonics, 3 014004 2021. https://doi.org/10.1088/2515-7647/abcbe4.

[9] C.V. Lopez, C.S. Salazar, K. Kells, J.C. Pedraza, and J.M. Ramos, Improving 3D reconstruction accuracy in wavelet transform profilometry by reducing shadow effects. IET Image Processing, 14, 310–317, 2020. https://doi.org/10.1049/iet-ipr.2019.0854.

[10] Y. Xu, H. Zhao, H. Jiang, and X. Li, High-accuracy 3D shape measurement of translucent objects by fringe projection profilometry. Optics Express, 27 (13),

18421-18434, 2019. https://doi.org/10.1364/OE.27.018421.

[11] C. Pérez, M. Chávez, F. C. Rivera, D. Sarocchi, C. Mares, and B. Barrientos, Fringe Projection Method for 3D High-Resolution Reconstruction of Oil Painting Surfaces. Heritage, 6 (4), 3461–3474, 2023. https://doi.org/10.3390/heritage6040184.

[12] Z. Yin, C. Liu, C. Zhang, X. He, and F. Yang, Point-Wise Phase Estimation Method in Fringe Projection Profilometry under Non-Sinusoidal Distortion. Sensors, 22 (12), 4478, 2022. https://doi.org/10.3390/s22124478.

[13] S. Lv, D. Tang, X. Zhang, D. Yang, W. Deng, and K. Qian, Fringe projection profilometry method with high efficiency, precision, and convenience: theoretical analysis and development. Optics Express, 30(19), 33515-33537, 2022. https://doi.org/10.1364/OE.467502.

[14] H. Kaya, Z. Saraç, M. Özer, and H. Taşkın, Optical signal processing of interference fringes by Hartley transform method. 17th Slovak-Czech-Polish Optical Conference on Wave and Quantum Aspects of Contemporary Optics, 77461W, Liptovsky Jan, Slovakia, 14-16 December 2010.

[15] B. Li, C. Tang, X. Zhu, Y. Su, and W. Xu, Shearlet transform for phase extraction in fringe projection profilometry with edges discontinuity. Optics and Lasers in Engineering, 78, 91–98, 2016. https://doi.org/10.1016/j.optlaseng.2015.10.007.

[16] A. Dursun, S. Özder, and F. N. Ecevit, Continuous wavelet transform analysis of projected fringe patterns. Measurement Science and Technology, 9(15), 0957-0233, 2004. 10.1088/0957-0233/15/9/013.

[17] J. Salvi, S. Fernandez, T. Pribanic, and X. Llado, A state of the art in structured light patterns for surface profilometry. Pattern Recognition. 43. 2666-2680 2010. https://doi.org/10.1016/j.patcog.2010.03.004.

[18] R. W. Wygant, S. P. Almeida, and O. D. D. Soares, Surface inspection via projection interferometry. Applied Optics, 27 (22), 4626-4630, 1988. https://doi.org/10.1364/AO.27.004626.

[19] J. Zhong, and J. Weng, Spatial carrier-fringe pattern analysis by means of wavelet transform: wavelet transform profilometry. Applied Optics, 43 (26), 4993-4998, 2004. https://doi.org/10.1364/AO.43.004993.

[20] J. Zhou, Wavelet-aided spatial carrier fringe pattern analysis for 3-D shape measurement. Optical Engineering, 44 (11), 113602, 2005. https://doi.org/10 1117/1.2127887.

[21] Z. Saraç, H. G. Birkök, H. Taşkın, and E. Öztürk, Evaluation of thermal lens fringes using Hilbert and Fourier transform methods. IET Science, Measurement and Technology, 5 (3), 81 – 87, 2011. https://www.researchgate.net/publication/224238898.

[22] C. Zuo, S. Feng, L. Huang, T. Tao, W. Yin, and Q. Chen, Phase shifting algorithms for fringe projection profilometry: A review. Optics and Lasers in Engineering, 109, 23-59, 2018. https://doi.org/10.1016/j.optlaseng.2018.04.019

[23] J. Geng, Structured-light 3D surface imaging: a tutorial. Advances in Optics and Photonics, 3 (2), 128–160, 2011. https://doi.org/10.1364/AOP.3.000128.

[24] H. A. Ali, M. A. Amer, and A. A. Omara, New Simple Large Depth of Field Fringe Projection Profilometry System Using Laser Projector. Journal of Measurement Science and Applications (JMSA), 2(2): 28-39, 2022.

[25] A. S. Segade, Fringe projection technique: New methods for shape measurement. Ph.D. Thesis, Centro de Investigaciones en Óptica A.C., Mexico, 2015.

[26] L. Mingzhou, Development of Fringe Analysis Techniques in white light interferometry for micro-component measurement. Ph.D. Thesis, National University of Singapore, Singapore, 2008.

[27] X. Su, and W. Chen, Fourier transform profilometry: a review. Optics and Lasers in Engineering, 35, 263–84, 2001.https://doi.org/10.1016/S0143-8166(01)00023-9.

[28] S. Zhang, and S-T. Yau, Generic nonsinusoidal phase error correction for three- dimensional shape measurement using a digital video projector. Applied Optics, 46 (1), 36–43, 2007. https://doi.org/10.1364/AO.46.000036.

[29] M. Takeda, and K. Mutoh, Fourier transform profilometry for the automatic measurement of 3D object shapes. Applied Optics, 22 (24), 3977–3982, 1983. https://doi.org/10.1364/AO.22.003977.

[30] A. Savitzky, M. J. E. Golay, Smoothing and differentiation of data by simplified least squares procedures. Analytical Chemistry, 36 (8), 1627–1639, 1964. https://pubs.acs.org/doi/10.1021/ac60214a047.

[31] P. A. Gorry, General lest-squares smoothing and differentiation by the convolution (Savitzky-Golay) method. Analytical Chemistry, 62, 570-573, 1990. https://pubs.acs.org/doi/abs/10.1021/ac00205a007.

[32] M. A. Awal, S. S. Mostafa, M. Ahmad, Performance analysis of Savitzky-Golay smoothing filter using ECG signal. International Journal of Computer and Information Technology, 1(02), 24, 2011. https://www.researchgate.net/publication/215628178.

[33] Q. Kemao, Two-dimensional windowed Fourier transform for fringe pattern analysis: Principles, applications and implementations. Optics and Lasers in Engineering, 45, 304-317, 2007. https://doi.org/10.1016/j.optlaseng.2005.10.012.

[34] Q. Kemao, Windowed Fourier transform for fringe pattern analysis. Applied Optics, 43 (13), 2695-702, 2004. https://doi.org/10.1364/AO.43.002695.

[35] S. Zheng, and Y. Cao, Fringe-projection profilometry based on two-dimensional empirical mode decomposition. Applied Optics, 52(31), 7648–7653, 2013. https://doi.org/10.1364/AO.52.007648.

[36] N.E. Huang, Z. Shen, S.R. Long, et al. The Empirical Mode Decomposition and the Hilbert Spectrum for Nonlinear and Non-Stationary Time Series Analysis. Proceedings of the Royal Society of London. Series A: Mathematical, Physical and Engineering Sciences, 454 (1971), pp. 903-995, Londra, England, 1998.

[37] W. Li, J. Huyan, S. L. Tighe, Q. Ren, and Z. Sun, Three-Dimensional Pavement Crack Detection

Algorithm Based on Two-Dimensional Empirical Mode Decomposition. Journal of Transportation Engineering, Part B: Pavements, 143 (2), 04017005, 2017. https://doi.org/10.1061/JPEODX.0000006.

[38] X. Zhou, G. Adrian, Z. Yang, T. Yang, and H. Zhao, Morphological operation-based bi- dimensional empirical mode decomposition for automatic background removal of fringe patterns. Optics Express, 20 (22), 24247–24262, 2012. https://doi.org/10.1364/OE.20.024247.

[39] S. Ertürk, Sayısal İşaret İşleme. 3rd ed., Birsen Yayınevi, Istanbul, 2016.